Available online at www.sciencedirect.com
SCIENCE DIRECT®
PERGAMON
International Journal of Heat and Mass Transfer 46 (2003) 3153–3166
International Journal of HEAT and MASS TRANSFER
www.elsevier.com/locate/ijhmt

Flow structure and local Nusselt number variations in a channel with angled crossed-rib turbulators

S.Y. Won, G.I. Mahmood, P.M. Ligrani *

Convective Heat Transfer Laboratory, Department of Mechanical Engineering, MEB 2202, 50 S. Central Campus Drive, University of Utah, Salt Lake City, UT, 84112-9208, USA

Received 5 February 2002; received in revised form 10 February 2003

Abstract

Spatially-resolved, local flow structure and surface Nusselt numbers are presented for a stationary channel with an aspect ratio of 4 and angled rib turbulators inclined at 45° with perpendicular orientations on two opposite surfaces. Instantaneous flow visualizations and time-averaged flow structural data show a variety of flow phenomena, including: (i) the development of increased numbers of multiple, smaller vortex pairs as the Reynolds number increases, and (ii) strong spanwise secondary flow components, which move in opposite directions in the top and bottom halves of the channel, and result in the formation of other secondary flows and vortical motions. The resulting increases in three-dimensional turbulence transport, as well as other flow phenomena, are then related to local Nusselt numbers, which vary significantly over the surface of the ribbed channel.

1. Introduction

The present study is conducted using a channel with aspect ratio of 4, with ribs oriented at 45° with respect to the streamwise flow direction, and placed perpendicular to each other on opposite sides of the two widest walls. This single-passage channel models internal cooling passages employed near the mid-chord and trailing edge regions of turbine airfoils used in gas turbine engines for utility power generation. Spatially-resolved flow structure (instantaneous and time-averaged), and along with examples of surface heat transfer coefficient distributions are presented. These flow field structural characteristics are obtained because they aid the development of numerical models and prediction schemes, and because they provide important insight into the flow phenomena responsible for local heat transfer coefficient augmentations. However, in spite of the value of flow structure data, obtained together with heat transfer data, very few papers present such data together for channels with rib turbulators.

Of the studies which consider flow structure in channels with rib turbulators, Bonhoff et al. [1] and Schabacker et al. [2] consider non-rotating channels, and Tse and Steuber [3], and Prabhu and Vedula [4] consider rotating channels. In one case, different velocity components are measured in a serpentine channel with 45° ribs [3], and in another, surface static pressure variations are measured with different channel aspect ratios, and different rotational speeds in a rectangular channel with traverse ribs on one wall [4]. Computational studies of flows in ducts with rib turbulators consider straight single pass ducts [5,8,9], two pass ducts [6,7,10], 90° orthogonal ribs [5,8], 45° angled ribs [6,7,9,10], and rotation [5–10]. The results from the most notable of these investigations with rotation show that the secondary flows induced by angled ribs, rotating buoyancy, and Coriolis forces produce strong non-isotropic turbulence stresses, along with important alterations to local and global flow field structure.

The present experimental study is conducted using a large-scale test section, without rotation, so that detailed, spatially-resolved flow structural characteristics

* Corresponding author. Tel.: +1-801-581-4240; fax: +1-801-585-9826.
E-mail address: ligrani@eng.utah.edu (P.M. Ligrani).

0017-9310/03/$ - see front matter © 2003 Elsevier Science Ltd. All rights reserved.
doi:10.1016/S0017-9310(03)00103-0

Nomenclature

a	streamwise extent of test surface
b	spanwise extent of test surface
D_h	channel hydraulic diameter
e	rib turbulator width
e'	rib turbulator width in streamwise direction
H	channel height
h	heat transfer coefficient based on flat projected area, $\dot{q}''_o/(T_w - T_m)$
k	thermal conductivity
Nu	local Nusselt number, hD_h/k
Nu_o	baseline Nusselt number in a smooth channel with no rib turbulators
p	streamwise pitch spacing of rib turbulators
P	time-averaged local static pressure
Pr	Prandtl number
$\dot{q}''_o$	surface heat flux
Re_H	Reynolds number based on channel height, $\overline{V}H/v$
Re_{D_h}	Reynolds number based on hydraulic diameter, $\overline{V}D_h/v$
t	time
t^*	non-dimensional time, $t\overline{V}/H$
T	local static temperature
u_x	time-averaged local streamwise component of velocity
u_y	time-averaged local normal component of velocity
u_z	time-averaged local spanwise component of velocity
$\overline{V}$	time- and spatially-averaged velocity across the channel cross-section
X	streamwise coordinate measured from the test section inlet
Y	normal coordinate measured from the test surface between the ribs
Z	spanwise coordinate measured from the test surface centerline

Greek symbols

ρ_a	air density at test section inlet
ω_x	streamwise vorticity

Subscripts

a	ambient value
i	test section inlet value
m	time-averaged, local mixed-mean value
o	total or stagnation value
w	local wall value

and surface Nusselt numbers can be measured. Reynolds numbers, based on channel height, range from 270 to 48,000. The results are new and unique because new spatially-resolved flow structure data and heat transfer data are inter-related to each other, something which is impossible for experimental rotating ribbed channel studies [3,4]. Included in the present study are: (i) time-sequences of flow visualization images, illustrating instantaneous flow structure, (ii) time-averaged distributions of local streamwise vorticity, local total pressure, local static pressure, and different components of local velocity, (iii) time-averaged distributions of secondary flow vectors and streamwise vorticity contours in a channel cross-sectional plane, and (iv) spatially-resolved surface Nusselt number data. The resulting picture, illuminated by these data, is of a complex, three-dimensional, time-varying flow field with significant flow losses and heat transfer augmentations.

2. Experimental apparatus and procedures

The overall experimental apparatus (but not the test section) is similar to the one described by Mahmood and Ligrani [11]. A brief description of this apparatus is also presented here.

2.1. Channel for flow structure measurements

A schematic diagram of the facility used for flow visualizations and flow structural measurements is shown in Fig. 1a. This facility is an open-loop, suction flow type of device. At the inlet of the facility, the air passes from the laboratory into a rectangular bell mouth inlet, followed by a honeycomb, two screens, and a two-dimensional nozzle with a contraction ratio of 5.6. This nozzles leads to a rectangular cross-section, 411 mm by 103 mm inlet duct which is 1219 mm in length, with an aspect ratio of 4. This is equivalent to 7.4 hydraulic diameters (where hydraulic diameter is 164.7 mm). Two trips are employed on the top and bottom surfaces of the inlet duct. Each of these is about 3 mm high, and extends across the span of the channel width, just upstream of the test section, which follows with the same cross-section dimensions and aspect ratio as the inlet duct. The test section exits to another smooth duct (which is about 0.315 m long with the same cross-section dimensions), which then connects to a 0.60 m square plenum, which is followed by two pipes, each containing an orifice plate. The pressure drop across one or the other of these orifice plates (measured using a Validyne M10 digital pressure manometer) is used to determine the air mass flow rate, using standard ASME procedures. The pipe then exits

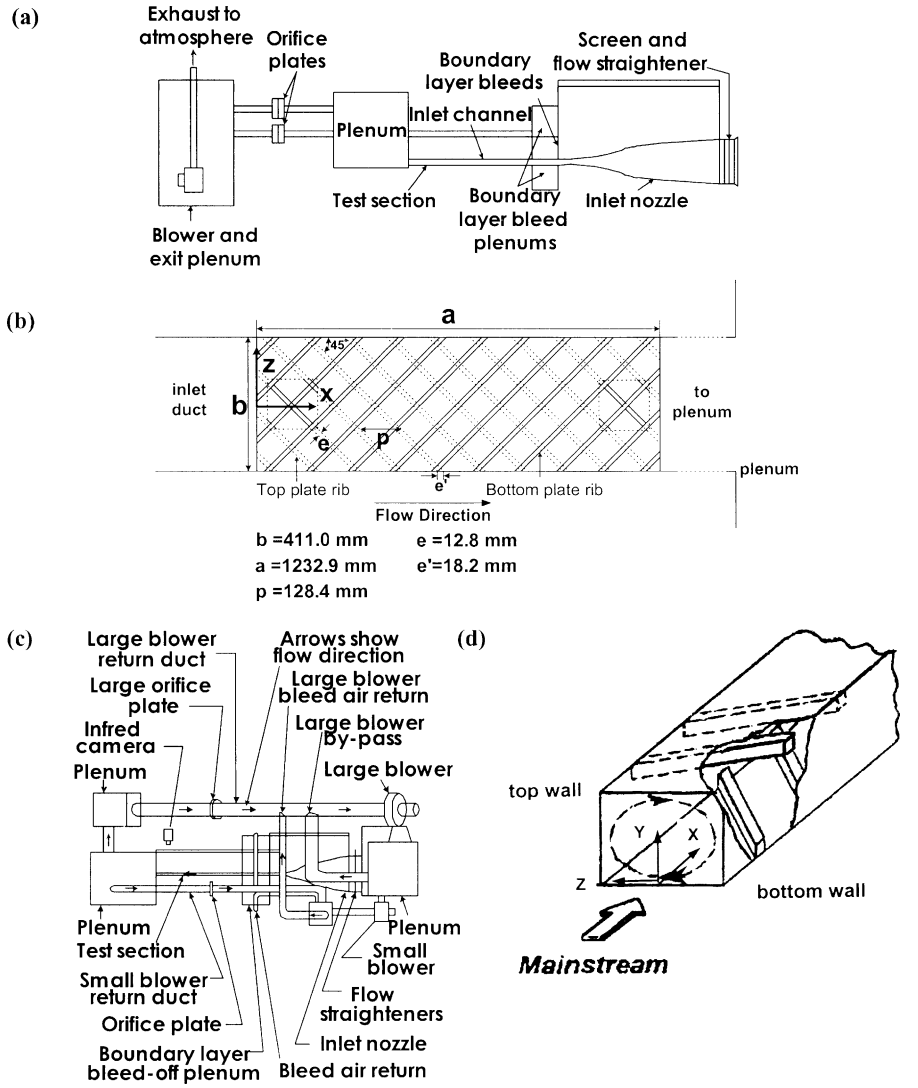

Fig. 1. Schematic diagrams of: (a) the experimental apparatus used for flow visualizations and measurements of flow structure, (b) the rib turbulator test surfaces, including coordinate system, (c) the experimental apparatus used for heat transfer measurements, and (d) overall flow pattern induced within a duct with arrays of cross-ribs angled at 45°.

into a second larger plenum, containing an ILG Industries type 10P centrifugal blower, which is employed to induce flow through the test section. From this second plenum, the air in the facility then exits to a vent.

2.2. Test surface geometry details

Fig. 1b gives the geometric details of the test surface, including rib turbulator geometry. A total of 13 acrylic ribs or rib segments are used on the top wall and on the bottom wall of the test section. As mentioned, these are arranged with 45° angles with respect to the streamwise flow direction, such that the ribs on opposite walls of the channel are perpendicular to each other. The ribs are arranged as shown in Fig. 1b, such that the ribbed test section is appended to the end of the smooth inlet duct. Each rib has 12.8 mm height and square cross-section. The ratio of rib height to hydraulic diameter is. 078, the rib pitch-to-height ratio is 10, and the blockage provided by the ribs is 25% of the channel cross-sectional area. The top wall of the test section also has two cut-out regions (one at the upstream end and one at the downstream end) where a zinc-selenide window can be installed to allow the infrared camera to view a portion of the test surface on the bottom wall. When this window is not in use, inserts with ribs (which exactly match the adjacent rib turbulators on the top wall) are used in its place. Also identified in Fig. 1b is the test section

coordinate system employed for the study. Note that the Y coordinate is directed normal to the bottom wall.

2.3. Time-averaged flow velocity components and pressure

A 1.27 mm diameter miniature five-hole pressure probe, manufactured at the University of Utah especially for these measurements, is used to obtain time-averaged surveys of total pressure, static pressure, and the three mean velocity components. These data are then used to deduce distributions of streamwise vorticity. To obtain the surveys, the probe employed is mounted on an automated two-dimensional traverse, and inserted into the test section through a slot lined with foam to prevent air leakage. The centerline of this probe is traversed as close as about 5 mm from the test section top wall, and as close as approximately 5 mm from the test section bottom wall. The output ports of the probe are connected either to Validyne DP103-06 pressure transducers (to measure differential pressures up to 2.5 mm of water), or Celesco LCVR pressure transducers (to measure differential pressures up to 20.0 mm of water). Signals from the transducers are then processed using Celesco CD10D Carrier-Demodulators. Voltages from the Carrier-Demodulators are acquired using a Hewlett-Packard 44422A data acquisition card installed in a Hewlett-Packard 3497A data acquisition control unit. This control unit, two Superior Electric type M092-FD310 Mitas stepping motors on the two-dimensional traverse, a Superior Electric Modulynx Mitas type PMS085-C2AR controller, and a Superior Electric Modulynx Mitas type PMS085-D050 motor drive are controlled by a Hewlett-Packard A4190A Series computer. Contour plots of measured quantities are generated using a polynomial interpolating technique between data points. In each survey plane, 1560 data points are spaced 2.54 mm apart. Data obtained at each one of these locations is time-averaged over a period of about 30 s. Additional details of the five-hole probe measurement procedures, including calibration details and procedures to account for velocity gradients and finite spatial resolution, are given by Ligrani et al. [12,13].

2.4. Flow visualization

Flow visualization using smoke is used to identify vortex structures and other secondary flow features. Smoke from four horizontally-oriented smoke wires is employed for this purpose. These are located 4.8, 11.9, 88.5, and 95.7 mm from the bottom test surface 25–29 mm from the downstream edge of the test section, which is equivalent to $X = 1258$–1261 mm. To accomplish this, each wire is first coated with Barts Pneumatics Corp. super smoke fluid and then powered using a Hewlett-Packard 6433B DC power supply. With this arrangement, the smoke forms into single thin lines parallel to the test surface. As the smoke is advected downstream, the secondary flows which accompany vortex and secondary flow development cause the smoke to be rearranged in patterns which show the locations and distributions of these flow phenomena. Smoke patterns are illuminated in a spanwise-normal light plane located at $X = 1462$ mm using a thin sheet of light provided by a Colotran ellipsoidal No. 550, 1000 W spot light, and a slits machined in two parallel metal plates. Images are recorded using a Panasonic WV-BP330 CCTV video camera, connected to a Panasonic AG-1960 type 4-head, multiplex video cassette recorder. Images recorded on video tape (taken individually or in sequence) are then digitized using a Sony DCR-TRV900 digital video camera recorder. The resulting images are then further processed using a Dell P4 Precision 330 PC computer. Additional discussion of many of the procedures used for flow visualization is provided by Ligrani [14].

2.5. Channel for heat transfer measurements

A separate channel facility (but with the same test section), and the same interior geometry identical to that in the flow structure facility, is employed for heat transfer measurements. A schematic drawing of this facility is shown in Fig. 1c. The air used within the facility is circulated in a closed-loop. One of three circuits is employed, depending upon the Reynolds number and flow rate requirements in the test section. For Reynolds numbers Re_H less than 10,000, a 102 mm pipe is connected to the intake of an ILG Industries 10P type centrifugal blower. For Re_H between 10,000 and 20,000, the same pipe is connected to the intake of a Dayton 7C447 1.0 hp centrifugal blower. For higher Reynolds numbers, a 203 mm pipe is employed with a New York Blower Co. 7.5 HP, size 1808 pressure blower. In each case, the air mass flow rate from the test section is measured (upstream of which ever blower is employed) using an ASME standard orifice plate and Validyne M10 digital pressure manometer. The blower then exits into a series of two plenums (0.9 m square and 0.75 m square). A Bonneville cross-flow heat exchanger is located between two of these plenums, and is cooled with liquid nitrogen at flow rate appropriate to give the desired air temperature at the exit of the heat exchanger. As the air exits the heat exchanger, it enters the second plenum, from which the air passes through the same types of flow management devices employed in the channel used for the flow structural measurements. These are followed by a 1219 mm long inlet duct, and the same test section used for the flow structural measurements.

All exterior surfaces of the facility (between the heat exchanger and test section) are insulated with Styrofoam ($k = 0.024$ W/m K), or 2 to 3 layers of 2.54 cm thick, Elastomer Products black neoprene foam insulation ($k = 0.038$ W/m K) to minimize heat losses. Calibrated copper-constantan thermocouples are located between the three layers of insulation located all around the test section to determine conduction losses. Between the first layer and the 3.2 mm thick acrylic test surfaces are custom-made Electrofilm etched-foil heaters (each encapsulated between two thin layers of Kapton). These provide a constant heat flux boundary condition on the inner faces of all four of the test surfaces employed in the test section. Surface heat flux rates of about 370 and 784 W/m^2 are employed for Re_H of 18,300 and 48,000, respectively. The acrylic surfaces, which are adjacent to the airstream, contain 35 copper-constantan thermocouples, which are placed within the ribs as well as within the flat portions of the test surface between the ribs. Each of these thermocouples is located 0.051 cm just below this surface to provide measurements of local surface temperatures, after correction for thermal contact resistance and temperature drop through the 0.051 cm thickness of acrylic. Acrylic is chosen because of its low thermal conductivity ($k = 0.19$ W/m K at 20 °C [15]) to minimize streamwise and spanwise conduction along the test surface, and thus, minimize "smearing" of spatially varying temperature gradients along the test surface. The power to the foil heater is controlled and regulated using a variac power supply. Energy balances, performed on the heated test surface, then allow determination of local magnitudes of the convective heat flux. These flux levels are based upon flat test surface areas.

The mixed-mean stagnation temperature of the air entering the test section is measured using five calibrated copper-constantan thermocouples spread across its cross-section. To determine this temperature, thermocouple-measured temperatures are corrected for thermocouple wire conduction losses, channel velocity variations, as well as for the differences between stagnation and recovery temperature. Magnitudes of mixed-mean temperature along the test surface are then determined using energy balances along with the measured mixed-mean temperature at the test section inlet. All measurements are obtained when the test facility is steady-state, achieved when each of the temperatures from the thermocouples (on the bottom test surface) vary by less than 0.1 °C over a 10 min period.

2.6. Local Nusselt number measurement

Spatially-resolved Nusselt number distributions along the bottom rib turbulator test surface are determined using infrared imaging in conjunction with thermocouples, energy balances, and in situ calibration procedures. To accomplish this, the infrared radiation emitted by the heated interior surface of the channel is captured using a VideoTherm 340 Infrared Imaging Camera, which operates at infrared wave lengths from 8 to 14 μm. Temperatures, measured using the calibrated, copper-constantan thermocouples distributed along the test surface adjacent to the flow, are used to perform the in situ calibrations simultaneously as the radiation contours from surface temperature variations are recorded. This is accomplished as the camera views the test surface through a custom-made, zinc-selenide window (which transmits infrared wave lengths between 6 and 17 μm) located on the top wall of the test section. The window is located just above portions of the tenth, eleventh, and twelfth ribs downstream from the leading edge of the test surface. The exact spatial locations and pixel locations of these thermocouple junctions and the coordinates of a 12.7 cm by 12.7 cm field of view are known from calibration maps obtained prior to measurements. During this procedure, the camera is focused, and rigidly mounted and oriented relative to the test surface in the same way as when radiation contours are recorded.

As measurements are made, images from the infrared camera are recorded as 8-bit gray scale images on commercial videotape using a Panasonic AG-1960 video recorder. Images are then digitized using NIH Image v1.60 software, operated on a Power Macintosh 7500 PC computer. Subsequent software is used to convert each of 256 possible gray scale values to local Nusselt number values at each pixel location using calibration data. Thermal conductivity in the Nusselt number is based on the temperature of the air at the test section inlet. Additional details of the infrared imaging and measurement procedures are provided by Sargent et al. [16], and Mahmood and Ligrani [11].

2.7. Uncertainty estimates

Uncertainty estimates are based on 95% confidence levels, and determined using procedures described by Kline and McClintock [17] and Moffat [18]. The experimental uncertainties of time-averaged magnitudes of local total pressure (relative to atmospheric pressure), local static pressure (relative to atmospheric pressure), local streamwise velocity, and local streamwise vorticity are ±4.0%, ±4.0%, ±2.5%, and ±8.0%, respectively. Uncertainty estimates of time-averaged magnitudes of the spanwise velocity component, and secondary flow vector magnitudes are about ±4.0%, and ±5.7%, respectively. Uncertainty of temperatures measured with thermocouples is about 0.2 °C. Spatial and temperature resolutions achieved with the infrared imaging are about 0.52 mm and 0.8 °C, respectively. This magnitude of temperature resolution is due to uncertainty in determining the exact locations of thermocouples with respect to pixel values used for the in situ calibrations. Local

Nusselt number ratio uncertainty is then about ±0.13 (for a ratio of 2.00), or about ±6.5%. Reynolds number uncertainty is approximately ±1.7% for Re_H of 10,000.

3. Experimental results and discussion

3.1. Local instantaneous flow structure

The overall secondary flows induced by the cross-rib arrangement are shown schematically in Fig. 1d from Cho et al. [19]. Noting the direction of the bulk flow, this figure shows that the 45° angled ribs act to induce strong secondary flow in the $+Z$ direction near the bottom wall, and in the $-Z$ direction near the top wall of the duct. The overall result is a single, large-scale cell of secondary, recirculating flow which encompasses the entire cross-section of the duct.

Visualizations of instantaneous flow behavior, obtained as part of the present study, show that other important secondary flows also develop in the duct, which are induced by the cross-ribs. A time-sequence of flow visualization images, which shows some of the secondary flows which are illuminated downstream of the ribbed test section at $X = 1462$ mm, is presented in Fig. 2a for $Re_H = 590$. These data are obtained at this low Reynolds number because diffusion and increased unsteadiness at higher Reynolds numbers result in smeared and unrecognizable flow patterns. Each image in Fig. 2a extends in the vertical direction from the bottom to the top of the channel, and in the horizontal direction over a distance of about 1.5 channel heights.

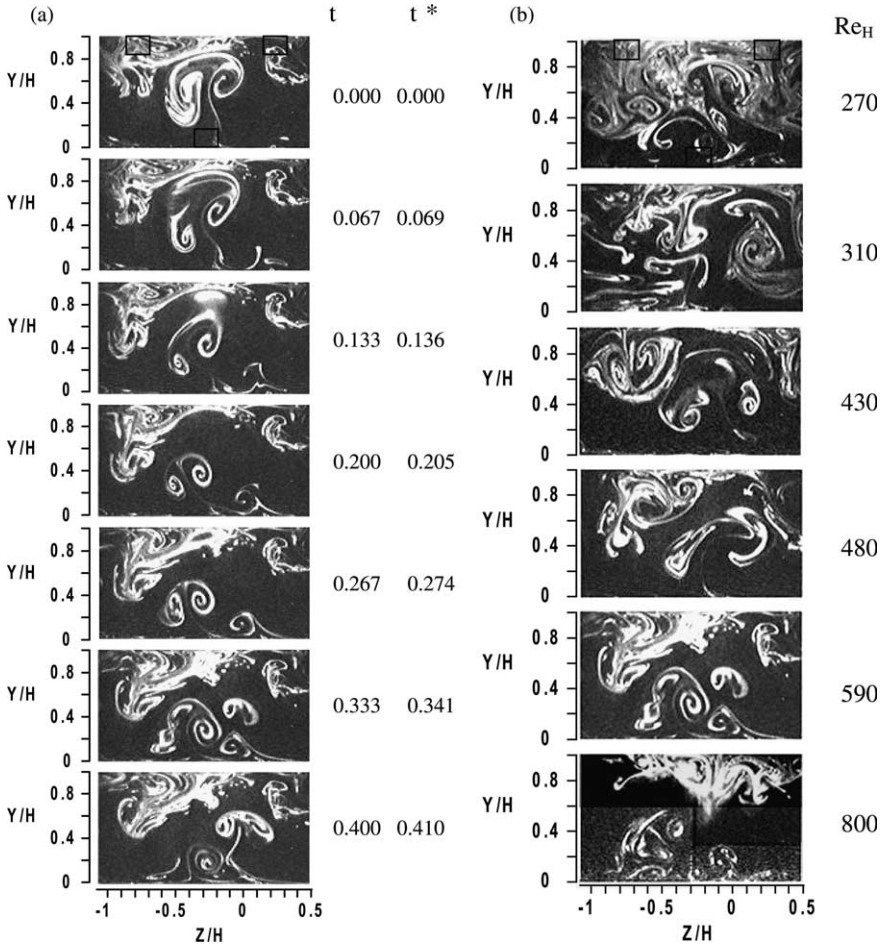

Fig. 2. Flow visualization images illuminated in a spanwise-normal plane at $X = 1462$ mm, including coordinate system locations. (a) Time-sequence of instantaneous flow visualization images for $Re_H = 590$. Rib locations are shown in the image corresponding to $t^* = 0.0$. (b) Instantaneous flow visualization images for different Reynolds numbers. Rib locations are shown in the image corresponding to $Re_H = 270$.

The coordinate system for each image is also shown in Fig. 2a.

Apparent in each image are multiple vortex pairs of different size (where each is indicated by a mushroom-shaped smoke pattern), which generally emanate from the bottom and top channel surfaces. These vortex pairs are formed by viscous effects, continuity, and the influences of the ribs, as they force air to and from the top and bottom test surfaces. Notice that the vortex pairs are often highly skewed, such that one vortex in each pair is larger than the other vortex. This is a result of the strong spanwise velocity components, which move in the $+Z/H$ direction near the bottom wall, and in the $-Z/H$ direction near the top wall, as mentioned. The vortex pairs change substantially with time, as indicated by different convolutions and distortions of smoke patterns in different images in Fig. 2a. The resulting complex, unsteady secondary flows (associated with the vortex pairs) are then present in conjunction with large-scale secondary flows, like the ones shown in Fig. 1d. Together, these act to continually rearrange distributions of streamwise velocity, so that shear gradients are spread over most of the channel cross-section.

Variations of instantaneous flow visualization images with Reynolds number are illustrated by the results presented in Fig. 2b. Here, two dominant vortex pairs, with opposite orientations, are generally present at Reynolds numbers Re_H from 270 to 480. The two primary vortex pairs at these conditions are sometimes located on opposite sides of the channel (at particular instants in time), with upwash regions directed in opposite directions (i.e. at $Re_H = 310$), or with the vortex pairs oriented diagonally with respect to each other (i.e. at $Re_H = 430$ and 480). At higher Re_H, these primary vortex pairs are then more convoluted and distorted, with larger numbers of smaller vortex pairs at the same channel locations where the larger primary pairs existed at lower Re_H. Fig. 2b thus provides some indication that larger-sized vortex pairs are generally replaced by collections of multiple, smaller vortex pairs as the Reynolds number increases. These data are obtained when the flow in the ribbed channel is mostly laminar (with pockets of turbulence only in certain locations). At higher Reynolds numbers, when the flow in the ribbed channel is fully turbulent, a similar variety of different flow structures are likely to be present, existing over a wide range of length scales. Such structures, and the vortices and secondary flows which accompany them, aid convective processes for turbulent heat transfer augmentation by: (i) increasing secondary advection of fluid between the central parts of the channel and regions near the wall, and (ii) producing regions with high, three-dimensional shear and high magnitudes of turbulence production over much of the channel cross-section, thereby substantially increasing turbulence transport levels in all three coordinate directions.

3.2. Local time-averaged flow structure

Time-averaged data also provide evidence of substantial secondary flows, significant mixing, and significant losses in the rib turbulated channel. Some of these data are presented in Figs. 3–6, which are measured at

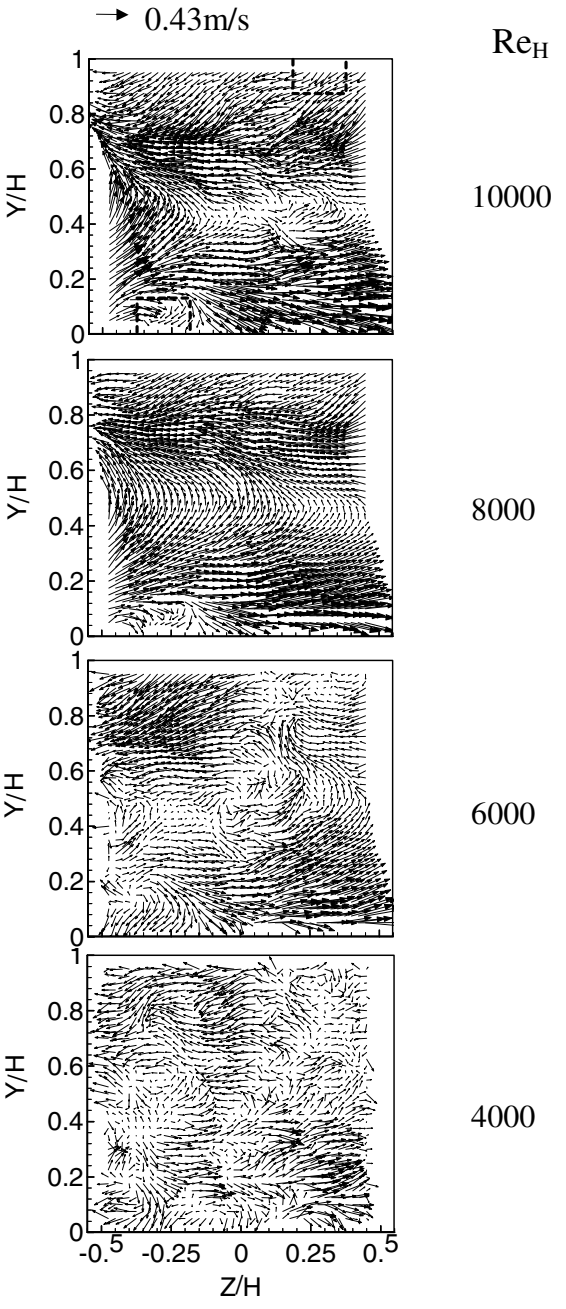

Fig. 3. Time-averaged secondary flow vectors in a spanwise-normal plane at $X = 1235$ mm for different Reynolds numbers Re_H, including coordinate system locations. Rib locations are shown in the image corresponding to $Re_H = 10{,}000$.

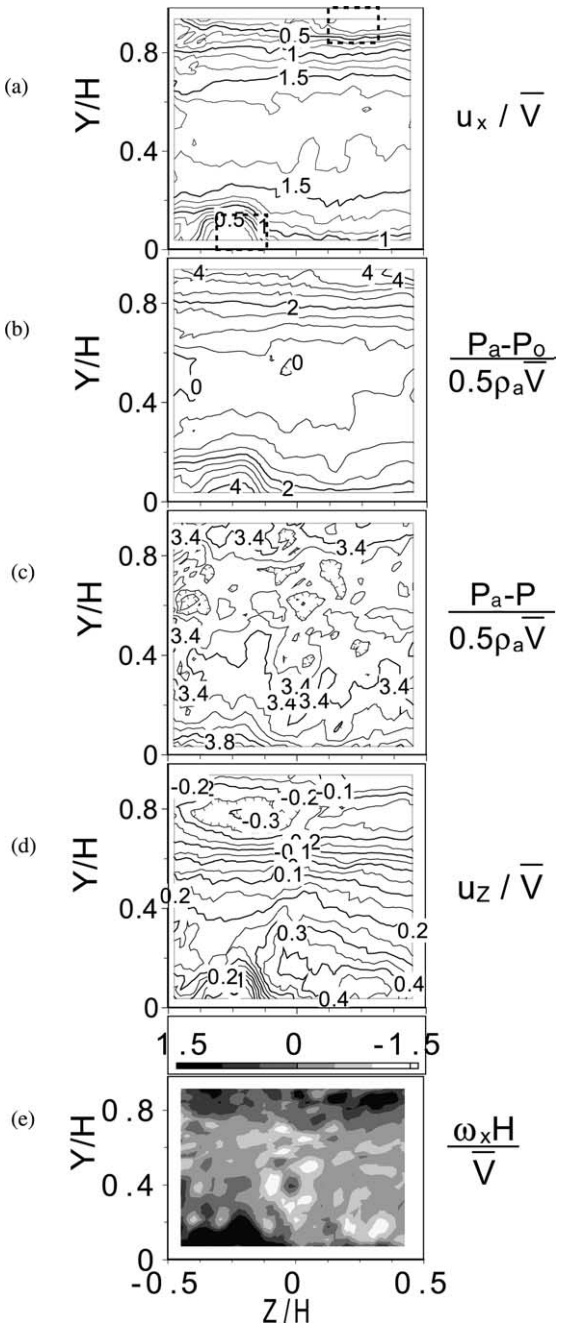

Fig. 4. Normalized, time-averaged surveys of: (a) local streamwise velocity, (b) local total pressure, (c) local static pressure, (d) local spanwise component of velocity, and (e) local streamwise vorticity from surveys conducted in a spanwise-normal plane at $X = 1235$ mm for $Re_H = 8000$. Rib locations are shown part (a).

$X = 1235$ mm, which is located just downstream of the test section, for Re_H of 4000, 6000, 8000, and 10,000. The surveys in the first two of these figures are made over a spanwise-normal plane, which extends about one channel height in each direction. The locations of the downstream ends of two of the ribs (one on the top surface and one on the bottom surface) are indicated in the first surveys at the tops of Figs. 3 and 4.

The intense secondary flows which are induced by the rib turbulators are illustrated by the results shown in Fig. 3a–d. Here, time-averaged magnitudes of secondary flow vectors are presented for different Re_H. Strong secondary flow vectors are evident, which generally move in the positive Z/H direction in the bottom half of the channel, and in the negative Z/H direction in the top half of the channel. This is consistent with the sketch of overall flow behavior shown in Fig. 1d. The magnitudes of the dimensional vectors in Fig. 3 (including the components in the spanwise directions) increase continually as the Reynolds number increases. Also apparent are swirls and vortical motions in the central part of the channel which are positioned between the strong secondary flows moving in the positive and negative Z/H directions. Another interesting feature are the flow diversions away from the wall in the vicinity of the ribs, whose downstream edges are positioned at the top-right and lower-left regions of each survey shown in Fig. 3.

The strong, spanwise secondary flows induce other smaller-scale, secondary flows in the channel. Some of these are evidenced by the streamwise vorticity distribution shown in Fig. 4e, which are deduced from the secondary flow vectors at $Re_H = 8000$, which are shown in Fig. 3b. The distribution of streamwise vorticity ω_x for $Re_H = 8000$, shown in Fig. 4e, shows several local positive regions near the top wall and several local negative regions near the bottom wall. Several regions with locally higher positive and negative vorticity are also evident across the entire channel cross-section near $Z/H = 0$. Such variations are qualitatively consistent with the flow visualization images in Fig. 2a and b. This is indicated by vortex pair upwash regions which are oriented in the same ways as some of the secondary flow vectors, and by visualized "mushroom petals", which are located at roughly the same positions as local fluid swirls and/or regions of higher streamwise vorticity.

Some of the secondary flows near the ribs give local regions of positive streamwise vorticity near the wall on the lesser Z/H side of the top rib (which is located at Z/H from 0.18 to 0.35), and local regions of negative streamwise vorticity near the wall on the higher Z/H side of the bottom rib (which is located at Z/H from −0.18 to −0.35). Also apparent in Fig. 4e are regions of mostly positive vorticity, immediately downstream of the downstream edges of a single rib on the bottom surface and a single rib on the top surface. The locations of these downstream rib edges are shown in Fig. 4a, as mentioned. Other small-scale secondary flows (in the form of local vortices and partial swirling motions) in Fig. 4e are induced by the large-scale secondary motions

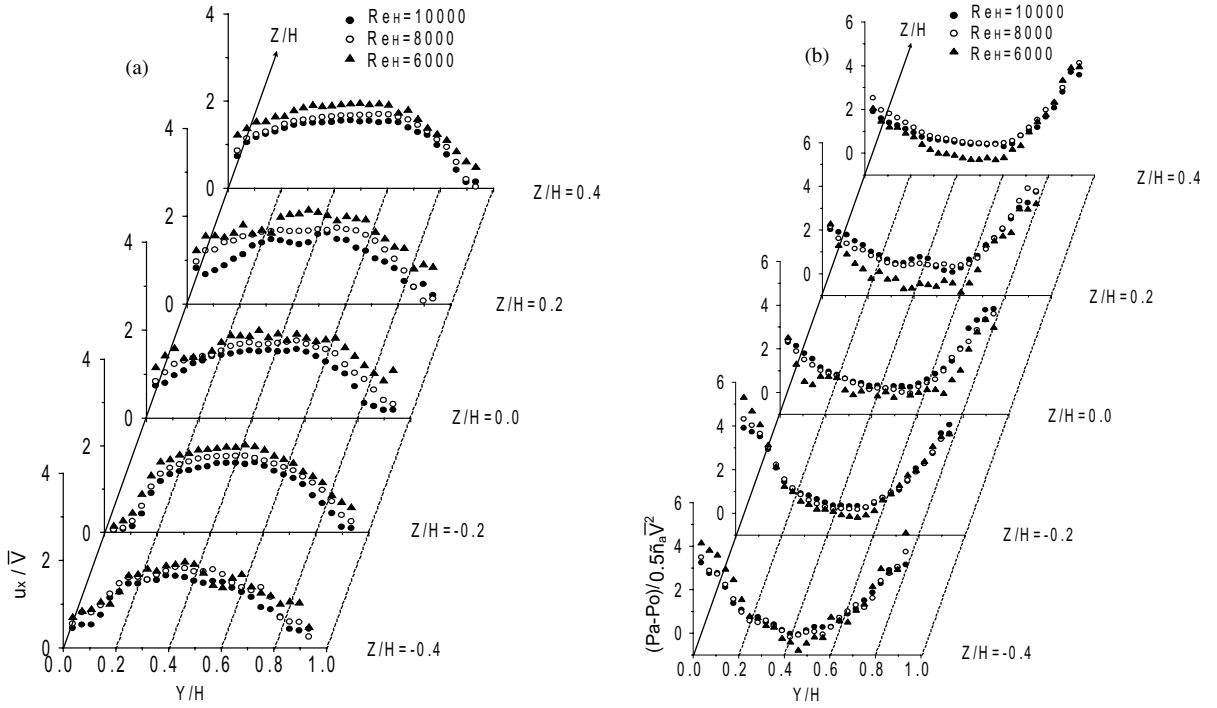

Fig. 5. Normalized profiles of: (a) local streamwise velocity, and (b) local total pressure at different Z/H positions from surveys conducted in a spanwise-normal plane at $X = 1235$ mm for Re_H of 6000, 8000, and 10,000.

in the spanwise directions. Continuity considerations are an important part of this development, and Kelvin–Helmholz shear layer instabilities may also play a role. Other data (not presented) show that vortices and partial swirls induced by such mechanisms are apparent across most of the channel cross-section near $Z/H = 0$ for Re_H from 4000 to 10,000. These are generally in the form of multiple, small regions of locally higher streamwise vorticity ω_x.

The normalized, time-averaged streamwise velocity data in Fig. 4a and the normalized, time-averaged total pressure data in Fig. 4b both show distributions which are nearly spanwise uniform. Such behavior is consistent with the presence of a large degree of unsteadiness in the flow. This is because the secondary advection, associated with such unsteadiness, continually rearranges and alters the positions of the vortices and other large-scale secondary flows in the channel. As a result, their signatures are smeared in data which is time-averaged at one channel cross-section location. Distributions of normalized $P_a - P_o$ in Fig. 4b also show that substantial losses are present in the channel, especially near the ribbed walls, considering that the kinetic energy, based on average velocity at this Reynolds number, is about 1.1 Pa. Note that local alterations to total pressure and streamwise velocity magnitudes are also evident in Fig. 4a and b (in the lower left and upper right parts of each survey), which are due to the downstream portions of two ribs.

The static pressure distribution in Fig. 4c also generally shows larger deficits near the channel walls. Other, additional local variations with the central part of the channel are also evident, which are mostly due to some local curvature of streamlines in the time-averaged flow field.

The survey of time-averaged spanwise velocity component u_z in Fig. 4d indicates that this secondary flow component is generally moving in the $+Z/H$ direction near the bottom wall and in the $-Z/H$ direction near the top wall. This is a result of the large-scale circulating flows induced by the ribs, mentioned earlier. Such fluid motions increase shear levels in the central part of the channel, and are due to the inclinations of the ribs with respect to the $+X$ direction, as well as the opposite rib orientations on the top and bottom surfaces of the channel.

Note that $\overline{V}$, the time-averaged velocity which is spatially-averaged over the channel cross-section, is used to normalize the data in Fig. 4, as well as the data which are presented in subsequent figures. This is the same velocity which is used to deduce the Reynolds number Re_H. It is generally slightly lower than values deduced

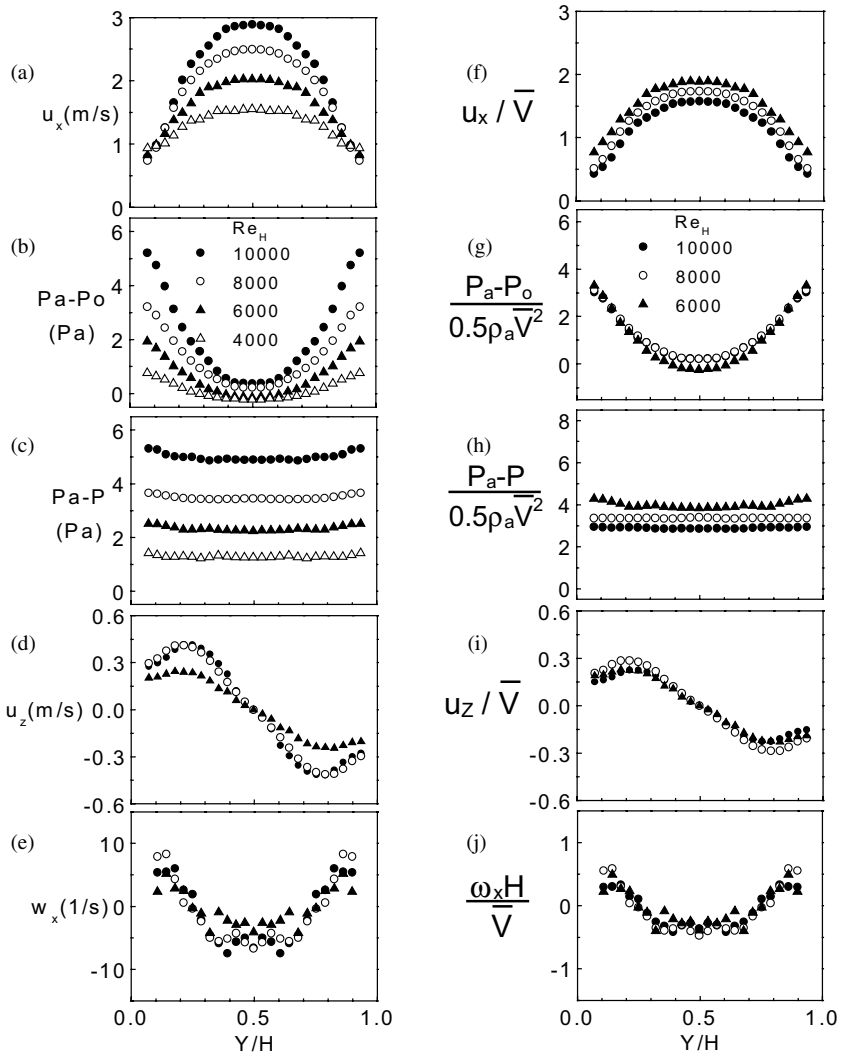

Fig. 6. Spanwise-averaged and time-averaged profiles of: (a) local streamwise velocity, (b) local total pressure, (c) local static pressure, (d) local spanwise component of velocity, (e) local streamwise vorticity, (f) normalized local streamwise velocity, (g) normalized local total pressure, (h) normalized local static pressure, (i) normalized local spanwise component of velocity, and (j) normalized local streamwise vorticity from surveys conducted in a spanwise-normal plane at $X = 1235$ mm for different Reynolds numbers Re_H.

from averaging locally-measured u_x values because local values are not measured in immediate vicinity of the ribbed walls, where values are lowest.

Additional information on local variations of normalized streamwise velocity, $u_x/\overline{V}$, and normalized total pressure, $(P_a - P_o)/0.5\rho_a\overline{V}^2$ is presented in Fig. 5a and b. Here, profiles of each of these quantities are presented for different Z/H and different Re_H. These data are determined from results like the ones shown in Fig. 4, which are measured at $X = 1235$ mm, which is located just downstream of the test section. Larger deficits of normalized streamwise velocity and normalized total pressure are present in the vicinity of the ribs, which (at this streamwise location) are located between $Z/H = -0.18$ and -0.35 on the bottom wall ($Y/H = 0.0$), and between $Z/H = +0.18$ and $+0.35$ on the top wall ($Y/H = 1.0$). Relative to spatially-averaged values, variations of normalized static pressure variations with Y/H are smaller, than variations of total pressure and streamwise velocity, with no significant changes in the vicinity of the ribs.

Fig. 6a–j then show how spanwise-averaged profiles of streamwise velocity, total pressure, static pressure, spanwise velocity, and streamwise vorticity vary with Reynolds number. Dimensional magnitudes are given in parts a–e and non-dimensional magnitudes are pre-

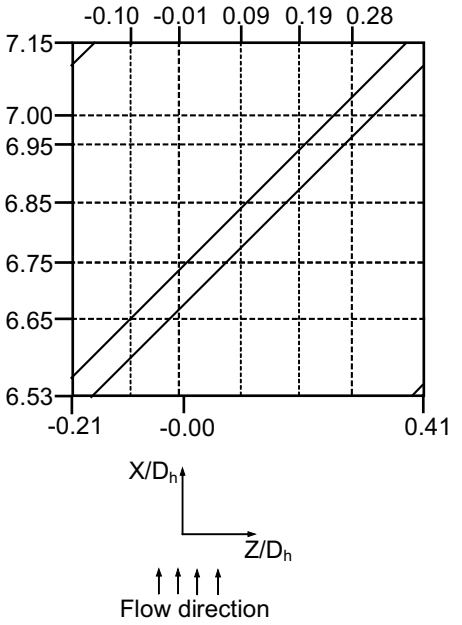

Fig. 7. Layout of the test surface showing the region where spatially-resolved surface Nusselt numbers are measured, including rib turbulator locations and lines along which data in Fig. 8a and b are presented.

sented in parts f–j. Each data point in each profile is obtained by averaging survey data in the Z/H direction as Y/H is held constant. Dimensional magnitudes of streamwise velocity u_x, total pressure $P_a - P_o$, and static pressure $P_a - P$ (in Fig. 6a–c) all generally increase with Reynolds number at each value of Y/H. The only exceptions are evident at $Y/H > 0.90$ and $Y/H < 0.10$, where the streamwise velocity data show the opposite trend. Magnitudes of the spanwise velocity component in Fig. 6d are generally much higher than normal component magnitudes. Spanwise velocity component profiles at the two highest Reynolds numbers (8000 and 10,000) are very similar, with slightly different behavior than measurements made at lower values of Re_H. Spanwise-averaged magnitudes of streamwise vorticity in Fig. 6e are positive near the walls and negative near the center of the channel, with roughly similar distributions for Re_H of 6000, 8000, and 10,000. The profiles in Fig. 6f–j show smaller variations with Reynolds number, since data are more closely collapsed together when presented in normalized form.

3.3. Local Nusselt number variations

Fig. 7 shows a schematic diagram of the rib turbulator test surface where local Nusselt number data are measured. Rib locations on the bottom wall are shown, along with lines of constant X/D_h and Z/D_h, which correspond to locations where local Nu/Nu_o data are given in Fig. 8a and b. In both of these figures, results are shown for Re_H of 18,300 and 48,000, and T_{oi}/T_w of

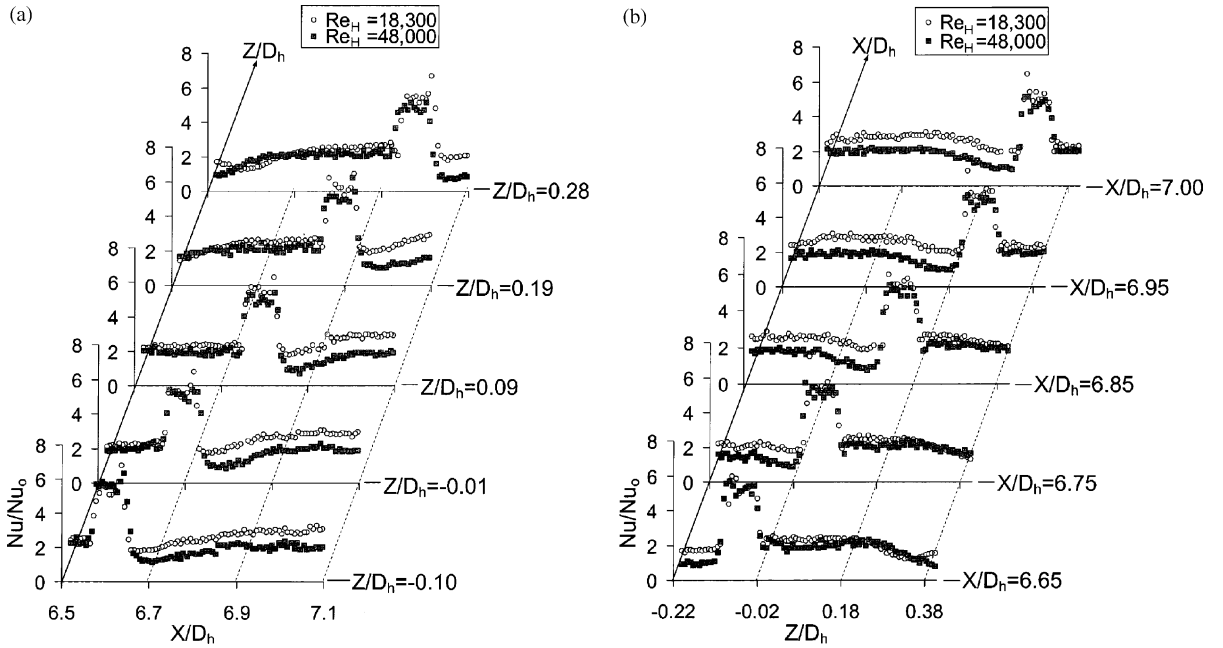

Fig. 8. Local Nusselt number ratios Nu/Nu_o for $Re_H = 18{,}300$ and 48,000, and a ratio of inlet stagnation temperature to wall temperature of 0.95. Data are given: (a) as they vary with X/D_h at Z/D_h of −0.10, −0.01, 0.09, 0.19, and 0.28, and (b) as they vary with Z/D_h at X/D_h of 6.65, 6.75, 6.85, 6.95, and 7.0.

0.93–0.95. The bulk flow direction is in the direction of positive X/D_h. Both data sets are time-averaged, determined from 25 instantaneous data sets acquired over a period of 25 s. Note that $Nu/Nu_o = 1$ in Fig. 8a and b corresponds to a channel with smooth walls (and no ribs) on all four surfaces. For this situation, baseline Nusselt numbers Nu_o are determined using an equation given by

$$Nu_o = 0.023 Re_{D_h}^{0.8} Pr^{0.4} \quad (1)$$

which is valid when uniform heat flux is applied to all four channel surfaces, and the channel flow is hydraulically and thermally fully developed.

Fig. 8a and b show that Nu/Nu_o ratios are relatively very high along the tops of the ribs. In both figures, rib tops are positioned at successively higher X/D_h and Z/D_h locations, as either Z/D_h or X/D_h increases. When compared along the rib tops, values are then often highest near the upstream and downstream edges. These values are determined by assuming that the uniform heat flux produced by the etched-foil heater leaves the test surface and enters the air stream from the top of the ribs and from the flat surface between the ribs. This then also assumes that no thermal power leaves the vertical sides of the ribs. Analysis of the conduction along such a test surface [20] of course shows that a portion of the thermal power also leaves the rib sides, which would give lower heat fluxes and lower Nu/Nu_o values along the rib tops. The present approach (of neglecting heat flux levels on rib sides) is justified because values along the rib tops in Fig. 8a and b account for all of the thermal power which enters the ribs at their bases (where they connect to the rest of the test surface). This then gives more realistic estimates of the overall heat transfer augmentation capabilities of the ribbed test surfaces.

As one moves from the rib in the streamwise or $+X/D_h$ direction in Fig. 8a, local Nu/Nu_o values decrease, and then are low relative to other locations on the test surface. This is due to streamline separation and a re-circulating flow region just downstream of the rib, where flow direction next to the surface is opposite to the bulk flow direction. A region where Nu/Nu_o values increase gradually with X/D_h then follows at slightly higher X/D_h. This is due to reattachment of the shear layer, which is initially formed above the re-circulating flow region. In Fig. 8b, local Nu/Nu_o variations due to the re-circulation regions and shear layer reattachment zones (downstream of the ribs) are positioned at smaller (or more negative) Z/D_h values compared to rib locations. In both cases, decreases of local Nu/Nu_o values with increasing Re_H are evident, which are a consequence of increases in the size and strength of the re-circulation zone and shear layer (which forms just above it) as the Reynolds number increases. Because of the normalization employed, this means that the observed Nusselt number Nu increases with Reynolds number are slower than baseline Nu_o increases with Re_H on these flat parts of the test surface. However, regardless of the Reynolds number, the pattern of observed flow and surface Nusselt number variations continually repeats itself as additional ribs are encountered along the test surface. This is important because the relatively low Nu/Nu_o values beneath flow re-circulation zones correspond to potential "hot-spots" where surface temperatures are relatively high. Conduction analysis of the same rib configuration [20] shows that "hot-spots" are also potentially very important at corner locations where ribs meet the connecting base plate.

The local, time-averaged surface Nusselt number distributions on the rib turbulator surface are then mostly a result of three different physical effects. (i) Nusselt number augmentations (relative to a channel with all smooth walls) are due to increased levels of three-dimensional turbulence transport. This is enhanced by increased turbulence shear stress and turbulence production over much of the channel cross-section. Responsible for this are: (a) the secondary flows and vortices (such as the ones shown in Figs. 2–4), which exist over a range of length scales over the entire channel cross-section, and (b) the highly skewed boundary layers along the surface (especially between the ribs) caused by secondary flows like the ones shown in Figs. 1d and 3, which are induced by the inclinations of the ribs with respect to the bulk flow direction. (ii) Significant heat transfer augmentations are also present on the ribs (especially on the tops), which are partly due to re-initialization of the thermal boundary layer and a small re-circulation zone, which form here. The increase in surface heat transfer area provided by the ribs also makes a contribution to local Nusselt number augmentations. (iii) The re-circulation zones act to decrease local Nusselt numbers just downstream of the ribs, relative to other locations. However, values increase somewhat in shear layer re-attachment zones. The flows in the re-circulation zones make positive contributions to heat transfer augmentations by acting to induce other secondary flows in other parts of the channel.

4. Summary and conclusions

Spatially-resolved flow structure and surface Nusselt numbers are presented for a stationary channel with an aspect ratio of 4 and angled rib turbulators inclined at 45°, with perpendicular orientations on two opposite surfaces. The flow structure results include time-averaged distributions of local streamwise vorticity, different components of local velocity, local total pressure, local static pressure, and secondary flow vectors, as well as instantaneous flow visualization images. Results are given at different Reynolds numbers based on channel

height from 270 to 48,000, and ratios of air inlet stagnation temperature to surface temperature of about 0.95. The ratio of rib height to hydraulic diameter is. 078, the rib pitch-to-height ratio is 10, and the blockage provided by the ribs is 25% of the channel cross-sectional area.

Flow visualizations show that increased numbers of multiple, smaller vortex pairs develop in the channel as the Reynolds number increases, which implies that energetic flow structures with a wide range of length scales are present in the fully turbulent channel flow. Time-averaged data also provide evidence of substantial secondary flows, significant mixing, and significant losses. Of particular importance are strong spanwise secondary flow components, which move in opposite directions in the top and bottom halves of the channel. Dimensional magnitudes of these spanwise velocity components increase with Reynolds number, and result in the formation of important vortical motions, including ones in the central part of the channel, and ones to the sides of the ribs. All of these vortices and secondary flows not only act to increase secondary advection of heat away from surfaces, but also to increase three-dimensional turbulence production by increasing shear and creating gradients of velocity over significant flow volumes. These then give larger magnitudes of three-dimensional turbulence transport over significant portions of the flow fields.

Such increased transport acts with thermal boundary layer re-initialization and small flow re-circulation zones on the tops of the ribs, and flow separation and shear layer re-attachment (just downstream of the ribs) to produce widely varying surface Nusselt numbers over the surface of the rib turbulated channel. The highest spatially-resolved local Nusselt numbers are then present on tops of the rib turbulators. Nusselt numbers are then lower, and decrease on the flat regions, especially at locations just downstream of the ribs, as Reynolds number increases. Such changes are partially due to increases in the size and strength of the flow re-circulation region, and the shear layer associated with it, as the Reynolds number increases. However, regardless of these variations, local, spatially-resolved Nusselt number *ratios* are generally much higher than 1.0 on most of the test surface, irrespective of the Reynolds number. This includes portions of flat regions between the ribs, and indicates significant augmentations of local surface heat transfer rates.

Acknowledgements

The work presented in this paper was sponsored by the AGTSR Advanced Gas Turbine Research Program of the SCIES, the South Carolina Institute for Energy Studies of the US Department of Energy. Mr. Eli Comeau, and Mr. Arthur Fox helped in setting up the experimental apparatus employed in the investigation.

References

[1] B. Bonhoff, S. Parneix, J. Leusch, B.V. Johnson, J. Schabacker, A. Bolcs, Experimental and numerical study of developed flow and heat transfer in coolant channels with 45° ribs, Int. J. Heat Fluid Flow 20 (1999) 311–319.

[2] J. Schabacker, A. Bolcs, B.V. Johnson, PIV investigation of the flow characteristics in an internal coolant passage with 45° rib arrangement, ASME 44th International Gas Turbine and Aeroengine Congress and Exposition, Indianapolis, IN, ASME Paper No. 99-GT-120, 1999.

[3] D.G.N. Tse, G.D. Steubner, Flow in a rotating square serpentine coolant passage with skewed trips, ASME 42nd International Gas Turbine and Aeroengine Congress and Exposition, Orlando, FL, ASME Paper 97-GT-529, 1997.

[4] S.V. Prabhu, R.P. Vedula, Pressure drop distribution in a rotating rectangular channel with one ribbed surface, ASME Paper No. 97-AA-118, 1997.

[5] C. Prakash, R. Zerkle, Prediction of turbulent flow and heat transfer in a ribbed rectangular duct with and without rotation, ASME Trans.—J. Turbomach. 117 (2) (1995) 255–264.

[6] M.A. Stephens, T.I.-P. Shih, Computation of compressible flow and heat transfer in a rotating duct with inclined ribs and 180 degree bend, ASME 42nd International Gas Turbine and Aeroengine Congress and Exposition, Orlando, FL, ASME Paper No. 97-GT-192, 1997.

[7] T.I.-P. Shih, Y.-L. Lin, M.A. Stephens, M.K. Chyu, Flow and heat transfer in a ribbed u-duct under typical engine conditions, ASME 43rd International Gas Turbine and Aeroengine Congress and Exposition, Stockholm, Sweden, ASME Paper No. 98-GT-213, 1998.

[8] H. Iacovides, Computation of flow and heat transfer through a rotating ribbed passage, Int. J. Heat Fluid Flow 19 (1998) 393–400.

[9] Y.-J. Jang, H.-C. Chen, J.C. Han, Flow and heat transfer in a rotating square channel with 45° angled ribs by Reynolds stress turbulence model, ASME 45th International Gas Turbine and Aeroengine Congress and Exposition, Munich, Germany, ASME Paper No. 2000-GT-229, 2000.

[10] M. Al-Qahtani, Y. Jang, H.C. Chen, J.C. Han, Prediction of flow and heat transfer in rotating two-pass rectangular channels with 45° rib turbulators, ASME 46th International Gas Turbine and Aeroengine Congress and Exposition, New Orleans, LA, ASME Paper No 2001-GT-187, 2001.

[11] G.I. Mahmood, P.M. Ligrani, Heat transfer in a dimpled channel: combined influences of aspect ratio, temperature ratio, Reynolds number, and flow structure, Int. J. Heat Mass Transfer 45 (10) (2002) 2011–2020.

[12] P.M. Ligrani, B.A. Singer, L.R. Baun, Miniature five-hole pressure probe for measurement of three mean velocity components in low speed flow, J. Phys. E—Sci. Instrum. 22 (10) (1989) 868–876.

[13] P.M. Ligrani, B.A. Singer, L.R. Baun, Spatial resolution and downwash velocity corrections for multiple-hole pressure probes in complex flows, Exp. Fluids 7 (6) (1989) 424–426.
[14] P.M. Ligrani, Flow visualization and flow tracking as applied to turbine components in gas turbine engines, Meas. Sci. Technol. 11 (7) (2000) 992–1006.
[15] F. Kreith, M.S. Bohn, Principles of Heat Transfer, fourth ed., Harper & Row, New York, 1986.
[16] S.R. Sargent, C.R. Hedlund, P.M. Ligrani, An infrared thermography imaging system for convective heat transfer measurements in complex flows, Meas. Sci. Technol. 9 (12) (1998) 1974–1981.
[17] S.J. Kline, F.A. McClintock, Describing uncertainties in single sample experiments, Mech. Eng. 75 (1953) 3–8.
[18] R.J. Moffat, Describing the uncertainties in experimental results, Exp. Therm. Fluid Sci. 1 (1) (1988) 3–17.
[19] H.H. Cho, S.Y. Lee, S.J. Wu, The combined effects of rib arrangements and discrete ribs on local heat/mass transfer in a square duct, ASME 46th International Gas Turbine and Aeroengine Congress and Exposition, New Orleans, LA, ASME Paper No. 2001-GT-175, 2001.
[20] G.I. Mahmood, P.M. Ligrani, Spatially-resolved heat transfer and friction factors in a rectangular channel with 45° angled crossed-rib turbulators, ASME Trans.—J. Turbomach. 125 (2003).